

A novel spaceborne SAR wide-swath imaging approach based on Poisson disk-like nonuniform sampling and compressive sensing

SUN JinPing*, ZHANG YuXi, TIAN JiHua & WANG Jun

School of Electronic and Information Engineering, Beihang University, Beijing 100191, China

Received November 21, 2011; accepted March 13, 2012; published online May 25, 2012

Abstract Since the range swath width in the conventional single channel spaceborne synthetic aperture radar (SAR) is restricted by the system parameters, there is a trade-off between the azimuth resolution and the swath width in order to satisfy the Nyquist sampling criterion. In this paper, we propose a novel spaceborne SAR wide-swath imaging scheme based on compressive sensing (CS) for the sparse scene. The proposed method designs a Poisson disk-like nonuniform sampling pattern in the azimuth direction, which meets the demand of wider swath by restricting the smallest time interval between any two azimuth samples, with the conventional sampling pattern preserved in the range direction. By a similar way to the processing procedure of spectral analysis (SPECAN) algorithm, the linear range migration correction (RMC) is realized while carrying out range compression, which can meet the demand for focusing with middle level resolution. To reduce the computation load of CS reconstruction, we propose a novel fast reconstruction algorithm based on nonuniform fast Fourier transform (NUFFT), which greatly reduces the computation complexity from $\mathcal{O}(2MN)$ to $\mathcal{O}(4N \log N)$. Experiment results validate the effectiveness of the proposed methods via the point target simulation and the Radarsat-1 raw data processing in F2 mode.

Keywords SAR, wide-swath imaging, compressive sensing, NUFFT

Citation Sun J P, Zhang Y X, Tian J H, et al. A novel spaceborne SAR wide-swath imaging approach based on Poisson disk-like nonuniform sampling and compressive sensing. *Sci China Inf Sci*, 2012, 55: 1876–1887, doi: 10.1007/s11432-012-4590-y

1 Introduction

As a well-proven imaging technique for remote sensing, spaceborne synthetic aperture radar (SAR) has been widely used for both civil and military applications. Modern spaceborne SAR systems demand imagery with both wide coverage and fine spatial resolution simultaneously. However, since the range swath width in the conventional single channel spaceborne SAR is restricted by the system parameters, there is a trade-off between the azimuth resolution and the swath width in order to satisfy the Nyquist sampling criterion [1]. And the modern spaceborne SAR wide-swath imaging systems generally adopt the flexible digital beamforming (DBF) or waveform coding techniques of phased array radars, both of which increase the system complexity in various degrees and are still realized under Nyquist sampling criterion [1–3]. The new concept of compressive sensing (CS) states that an unknown sparse (or sparse under some

*Corresponding author (email: sunjinping@buaa.edu.cn)

transform-domain) signal can be recovered even from what appear to be highly sub-Nyquist-rate samples by solving an l_1 -optimization problem [4,5], thus offering the possibility of realizing wider swath for conventional single channel spaceborne SAR system for sparse scenes such as sea. CS theory can effectively reduce the system complexity in acquiring image technique and has been already applied to the radar imaging techniques [6–11]. In existing literature, the azimuth under sampling pattern in SAR imaging based on CS is typically designed as the random selection strategy, but this method cannot be applied to wide-swath imaging in spaceborne SAR since it is unable to ensure that the time interval between any two adjacent samples is smaller than the one under the Nyquist limitation. At this point, we propose a Poisson disk-like nonuniform sampling pattern in the azimuth direction, which satisfies the demand of wider swath with the constraint of the smallest interval between any two azimuth samples. As to range migration correction (RMC) of imaging procedure, the linear RMC is realized while carrying out range compression through a way similar to the processing procedure of spectral analysis (SPECAN) algorithm [12], which can meet the demand for focusing with middle level imagery resolution. After RMC, azimuth focusing of SAR imagery can be taken as a CS reconstruction procedure. Current widely used CS reconstruction methods include iterative greedy algorithms, such as orthogonal matching pursuit (OMP), regularized OMP (ROMP), convex relaxation algorithms such as iterative shrinkage/thresholding (IST) [13], gradient projection for sparse reconstruction (GPSR) and so on. All the above reconstruction algorithms have the huge computational complexity with large scale problems, and this puts strict constraint on practical CS radar applications. Particularly, the most computationally expensive parts in CS algorithms are the matrix-vector products. In this paper, we propose a novel fast reconstruction algorithm by substituting the costly matrix-vector multiplication with fast Fourier transform (FFT) and nonuniform FFT, i.e., NUFFT. The method greatly reduces the computation complexity from $\mathcal{O}(2MN)$ to $\mathcal{O}(4N \log N)$ and therefore speeds up the azimuth focusing procedure of proposed CS based SAR imagery method. The remainder of this paper is organized as follows. In Section 2, we present the design of Poisson disk-like nonuniform sampling pattern in the azimuth direction. In Section 3, SAR imaging processing based on CS is described in detail. The new NUFFT-IST fast reconstruction algorithm is presented in Section 4, and experiment results of the point target simulation and the Radarsat-1 raw data processing are presented in Section 5. Some conclusions are drawn in the last section.

2 Nonuniform azimuth sampling pattern design

2.1 Theory of compressive sensing

Compressive sensing is a new promising theory that enables accurate recovery of signals and data from what appear to be highly sub-Nyquist-rate samples [4,5] as long as the signal is compressible or sparse in a certain transform domain. The core idea of compressed sensing is described briefly as follows:

Suppose that a signal $\mathbf{x} \in \mathbb{R}^N$ is K -sparse on an orthonormal basis Ψ , i.e.,

$$\mathbf{x} = \Psi \mathbf{s}, \quad (1)$$

where $\Psi = \{\psi_1, \psi_2, \dots, \psi_N\}$ is an $N \times N$ matrix constructed by sparse basis $\{\psi_n\}$, and \mathbf{s} is a vector with all except $K \ll N$ of its entries are zeros. In CS framework, the measurements $\mathbf{y} \in \mathbb{R}^M$ ($M < N$) are obtained through a non-adaptive linear projection, mathematically

$$\mathbf{y} = \Phi \mathbf{x} = \Phi \Psi \mathbf{s}, \quad (2)$$

where Φ is an $M \times N$ measurement matrix.

Since $M < N$, recovery of \mathbf{x} from \mathbf{y} is ill-posed. However, CS theory states that when the matrix $\mathbf{A} = \Phi \Psi$ has the restricted isometry property (RIP), the signal \mathbf{s} can be recovered with high probability from a similarly sized set of $M = \mathcal{O}(K \log(N/K))$ measurements \mathbf{y} . When the RIP holds, the signal \mathbf{x} (via coefficient vector \mathbf{s}) can be recovered exactly by solving the l_1 minimization problem

$$\min \|\mathbf{s}\|_1 \quad \text{s.t.} \quad \mathbf{y} = \Phi \Psi \mathbf{s} \quad (3)$$

with linear programming techniques. Current widely used reconstruction methods include OMP, ROMP, IST, GPSR, and so on.

2.2 Spaceborne SAR range swath restrictions due to sampling

For a given conventional single channel spaceborne SAR system, the relation between azimuth resolution and Doppler bandwidth caused by platform motion can be expressed as $\rho_a = \kappa_a V_g / B_a$, where V_g denotes the ground speed of satellite, B_a represents the Doppler bandwidth, and κ_a refers to the broaden factor. The Doppler bandwidth is approximately $B_a = 2 \times 0.8859 V_s / d$, where V_s denotes the speed of satellite, and d is the size of radar antenna in azimuth direction. In order to meet the Nyquist sampling criterion, the azimuth sampling rate of SAR system, which refers to the pulse repetition frequency (PRF), must be higher than Doppler bandwidth, i.e.,

$$\text{PRF} \geq (1 + \kappa) B_a, \quad (4)$$

where κ is oversampling factor required to suppress azimuth ambiguities. Hence, the slant range swath width is restricted to

$$R_w \leq \left(\frac{1}{\text{PRF}} - 2T_p \right) \frac{c}{2}, \quad (5)$$

where T_p is the pulse duration, and c denotes the speed of light. Considering that the higher resolution needs wider Doppler bandwidth, and consequently requires higher PRF according to (4), the increasing PRF will inevitably decrease the range swath width. However, the new CS theory provides the possibility to break the restriction of (4), and accordingly makes it possible to obtain a wider range swath than the conventional operation.

2.3 Design of Poisson disk-like random sampling

Making use of the sparse characteristic of target scene, the main purpose of the spaceborne SAR wide-swath imaging scheme based on CS is to break the restriction of (4) in the azimuth direction, so the key problem is how to design a suitable azimuth sampling pattern. As a coherent pulse Doppler radar, the echo signal of SAR in pulse mechanism is discrete at the slow time direction (azimuth direction), which means the azimuth sparse sampling cannot be directly realized with the scheme of analog-to-information converter (AIC) [5], instead we should determine the correct azimuth sampling instants (the pulse transmission time sequence). **In the existing literature, the azimuth under sampling pattern in SAR imaging based on CS is typically designed as the random selection strategy, but this method cannot be applied to wide-swath imaging in spaceborne SAR since it is unable to ensure that the time interval between any two adjacent samples is smaller than the one under the Nyquist limitation, although it can efficiently reduce the number of echo samples.** Poisson disk sampling is commonly used in computer graphics, and it can simply and mathematically be defined as a set of samples (points) in a certain distance space such that every pair of samples are at least certain distance away from each other [14]. Poisson disk sampling has already been applied to compressed MRI as an optimal CS sampling pattern [15]. For the wide-swath imaging, to make sure no aliasing appears in the range direction, the smallest time interval between two adjacent pulses must follow $\Delta t_{\min} \geq (2R_w/c + 2T_p)$; as a result, the azimuth random sampling instant can be designed as

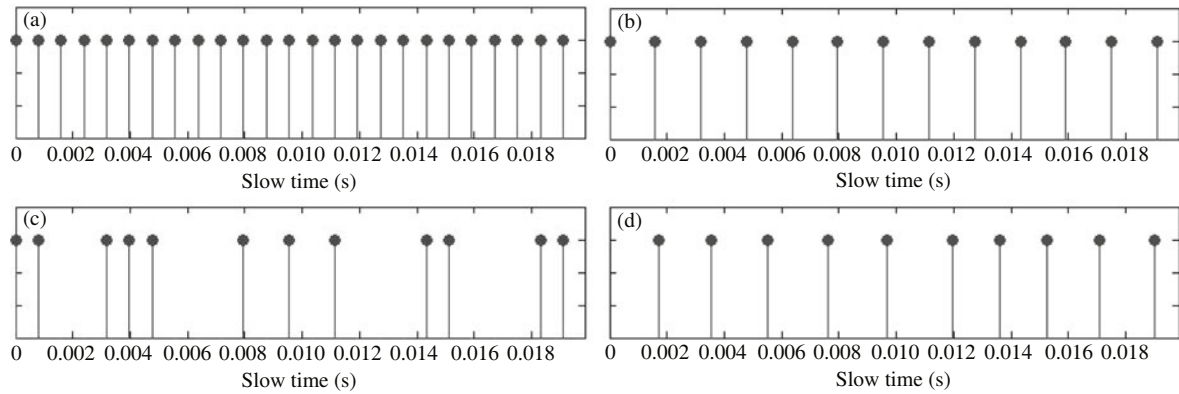
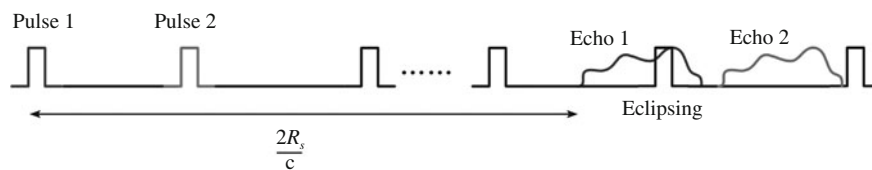
$$t_j = t_{j-1} + \left(\frac{2R_w}{c} + 2T_p \right) + \delta_t, \quad (6)$$

where R_w is the desired swath width, δ_t is a random variable uniformly distributed in the interval $[0, T_R]$, and $T_R = 1/\text{PRF}$ is pulse repetition period that meets Nyquist sampling criterion. Here, we stack the M azimuth sampling instants as a vector $\mathbf{t} = [t_0, t_1, \dots, t_{M-1}]^T$.

Taking the parameters of Radarsat-1 given in Table 1 for example, the PRF that meets Nyquist sampling criterion is 1256.98 Hz. Figure 1 shows the comparison of several different sampling patterns, where the Poisson disk-like sampling pattern is designed to double the swath width.

Table 1 System parameters

Parameter description	Value
Wave length	0.05657 m
Chirp bandwidth	30.111 MHz
Chirp duration	41.74 μ s
Sampling rate	32.317 MHz
Pulse repetition frequency	1256.98 Hz
Effective radar velocity	7062 m/s
Doppler centroid	−6900 Hz
Azimuth beam width	0.2°

**Figure 1** Comparison of different sampling patterns. (a) Uniform sampling pattern with PRF; (b) uniform sampling pattern with a down sampling rate PRF/2; (c) random selection nonuniform sampling pattern; (d) Poisson disk-like nonuniform random sampling pattern.**Figure 2** Effect of pulse eclipsing caused by Poisson disk-like random nonuniform sampling pattern.

The Poisson disk-like azimuth sparse sampling pattern for spaceborne SAR echo signal can guarantee that no aliasing appears between echo signals of two adjacent transmitted pulses. But the sampling of the corresponding echo signal of some transmitted pulse starts 4–6 pulses later than the pulse transmitted because of the long range between target scenes and spaceborne SAR platform, which will cause the random pulse eclipsing shown in Figure 2. Since the time interval between two transmitted pulses is a random variable distributed uniformly in some fixed interval, we cannot make sure no pulse is transmitted when sampling the echo signal of the n th pulse. The sampling operation will be interrupted if a new pulse is needed to be transmitted, and then the pulse eclipsing phenomenon happens. The time pulse eclipsing happens and the corresponding time duration is dependent on the system parameters, imagery geometry and the pre-designed Poisson disk-like sampling instants, which also show some random characteristic.

With the system parameters of Radarsat-1 in F2 mode, design the Poisson disk-like sampling pattern to double the swath width (the start slant range is $R_s = 980$ km, and the swath width is $R_w = 238.7$ km), and the number of azimuth sparse samples is 822. Then we can get the distribution of random pulse eclipsing in slow time and fast time directions. Figure 3 demonstrates the distribution of pulse eclipsing and also gives the number of eclipsed pulses in azimuth direction versus slant range. We can see that only very few eclipsings happen at different rang bins with parameters of Radarsat-1 in F2 mode, and

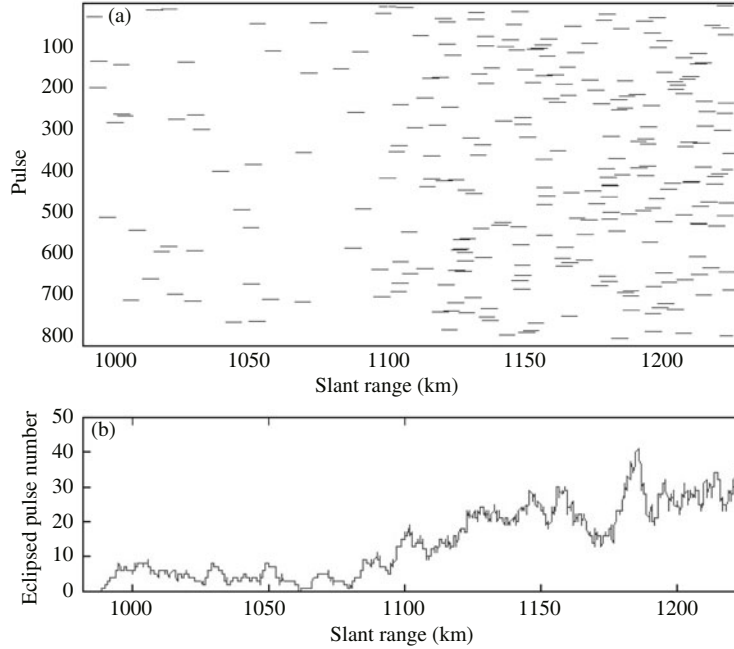


Figure 3 Calculation of pulse eclipsing with Radarsat-1 F2 mode parameters. (a) Eclipsing map for every pulse, short lines indicate eclipsed scopes of slant range; (b) eclipsed pulse number at different slant ranges.

the eclipsed pulse number is approximate to 40 at the most frequent point, the proportion of which to the total number of pulses is very small ($40/822 = 4.9\%$). The most important, since the eclipsing happens randomly, it can be seen as part of the nonuniformly random sampling pattern, and the few measurements lost have little impact on the results through CS reconstruction.

3 SAR imaging processing based on CS

Although the random CS sampling can theoretically reduce the data rate of every echo pulse, it will reduce the signal-to-noise ratio (SNR) in practice and the nonlinear CS recovery will cause phase distortion in the case of low input SNR; therefore we still adopt the conventional sampling pattern in the range direction. Moreover, because the two-dimension CS recovery with RMC needs a large cost of computation, we employ range-azimuth decoupling method, which can meet the demand for focusing with middle level resolution. In a similar way to the processing procedure of SPECAN algorithm, we can realize the linear RMC while carrying out range compression by utilizing the pre-designed sampling instants vector \mathbf{t} , when the Doppler centroid is nonzero. The detailed SPECAN algorithm for conventional spaceborne SAR imagery processing was presented in [12]. The proposed CS based spaceborne SAR wide-swath imaging processing flow is shown in Figure 4.

Suppose SAR system transmits linear modulation frequency (LFM) signal. Let K_r denote the chirp rate, the speed of platform along LOS be V_r , the Doppler centroid be f_{dc} in the synthetic aperture time, and let the range frequency be denoted by f_r . Then the reference phase function used for range compression and linear RMC at azimuth sampling instant t_j can be expressed as

$$H_1(f_r, t_j) = \exp\left(i\frac{\pi}{K_r}f_r^2\right) \exp\left(-i2\pi\frac{2V_r t_j}{c}f_r\right) \exp(-i2\pi f_{dc}t_j). \quad (7)$$

First, compute FFT of the original samples along range direction, and multiply the results with the corresponding reference phase function $H_1(f_r, t_j)$ at azimuth sampling instant t_j , and then compute the IFFT in range direction. Then we will complete the range compression and linear RMC.

After range compression and the linear RMC, we denote azimuth signal at slant range r by $y(r, t)$. The conventional azimuth compression through matched filtering at slant range r can be realized in the

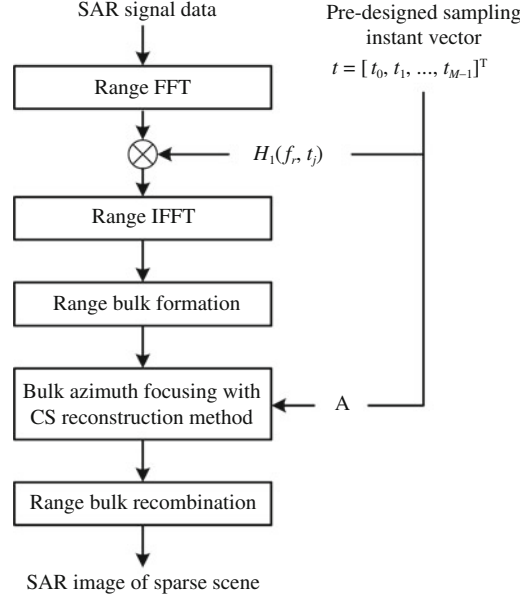


Figure 4 CS based spaceborne wide-swath SAR imaging processing flow.

range-Doppler domain. The output signal that represents the sparse scene is

$$s(r, t) = F^{-1}(Y(r, f_a) H(r, f_a)), \quad (8)$$

where f_a is the azimuth frequency, $Y(r, f_a) = F(y(r, t))$, and F with F^{-1} denotes Fourier transform and inverse Fourier transform operation respectively. Azimuth transfer function is

$$H(r, f_a) = \exp\left(i \frac{4\pi}{\lambda} r \sqrt{1 - \left(\frac{\lambda f_a}{2V_g}\right)^2}\right), \quad (9)$$

where λ is the wavelength, and the signal observation model corresponding to (8) is

$$y(r, t) = F^{-1}(F(s(r, t)) H^*(r, f_a)). \quad (10)$$

Here, $(\cdot)^*$ denotes the complex conjugate. The corresponding discrete form of the observation model is

$$\mathbf{y} = \mathbf{H}\mathbf{F}_v \mathbf{s} = \mathbf{A}\mathbf{s}, \quad (11)$$

where $\mathbf{A} = \mathbf{H}\mathbf{F}_v$, the echo samples are defined by $\mathbf{y} = [y(r, t_0), y(r, t_1), \dots, y(r, t_{M-1})]^T$, and $\mathbf{t} = [t_0, t_1, \dots, t_{M-1}]^T$ is the pre-designed nonuniform azimuth sampling instants vector. The desired sparse scene samples are defined by $\mathbf{s} = [s(r, 0), s(r, T_R), \dots, s(r, (N-1)T_R)]^T$, with the uniform space interval $\Delta_x = V_g T_R$ satisfying the Nyquist limitation. The $N \times N$ matrix $\mathbf{F}_v = [\mathbf{v} \odot \mathbf{f}_1, \mathbf{v} \odot \mathbf{f}_2, \dots, \mathbf{v} \odot \mathbf{f}_N]$, and \mathbf{f}_k is the k th column vector of discrete Fourier transform (DFT) matrix \mathbf{F} , and \odot denotes the Hadamard product. The discrete conjugate transfer function $\mathbf{v} = [v_1, v_2, \dots, v_N]^T$ with $v_n = H^*(r, f_n)$ and $f_n = \text{PRF}(n-1)/N$. The $M \times N$ nonuniform IDFT (NUIDFT) matrix $\mathbf{H} = [\mathbf{h}_1, \mathbf{h}_2, \dots, \mathbf{h}_N]$ transforms equally-spaced frequency samples to nonuniform signal samples with $\mathbf{h}_n = [e^{i2\pi t_0 f_n}, e^{i2\pi t_1 f_n}, \dots, e^{i2\pi t_{M-1} f_n}]^T$.

Since $M < N$, problem (11) is underdetermined. Fortunately, according to the CS theory, \mathbf{s} can be reconstructed by solving the optimization problem (3) with its characteristic of sparsity. We adopt the IST algorithm for the CS reconstruction in this paper, and modify the IST based on NUFFT technique, as will be described in next section. In the practical process of imaging, it will bring a large storage requirement and is not necessary if we construct a new CS matrix \mathbf{A} for each range bin. As shown in Figure 4, we can apply the range bulk formation strategy, i.e., construct a unitary CS matrix for a certain range of slant range bins. Azimuth transfer function of these range bins can be approximated according to the required resolution. And the fewer CS matrices are needed if the lower azimuth resolution is required.

4 NUFFT-IST fast reconstruction algorithm

4.1 NUFFT algorithm

NUFFT (nonuniform DFT) has a rapid development in the past two decades, and has already been widely applied to computational electromagnetics, radar imaging and other fields. Given a nonuniform set of signal samples $x(t_m)$, $m = 0, \dots, M-1$, NUDFT is defined by

$$X_k = \sum_{m=0}^{M-1} x(t_m) e^{-i2\pi t_m f_s k/N}, \quad k = 0, \dots, N-1, \quad (12)$$

where $t_m f_s \in [0, N)$, X_k is the uniform frequency samples.

The general idea of NUFFT algorithm is to first compute an oversampled FFT of the weighted form of the given signal samples and then carry out efficient interpolation for the desired samples.

Therefore, the procedure of approximating the nonuniformly-spaced signal samples via NUFFT can be expressed as

$$\hat{x}(t_m) = \sum_{j=0}^{J-1} z(k_m + j) u_j^*(t_m), \quad m = 0, \dots, M-1, \quad (13)$$

where $z(n) = \frac{1}{N} \sum_{k=0}^{N-1} a_k X_k e^{i2\pi n k/N}$, $n = 0, \dots, N-1$, a_k is the scaling factors, $u(t_m)$ is the interpolator with length of J , and the interpolation offset is given by

$$k_m = \begin{cases} \arg \min_{k \in \mathbb{Z}} |t_m - k/f_s| - (J+1)/2, & J \text{ odd}, \\ \max\{k \in \mathbb{Z} : t_m \geq k/f_s\} - J/2, & J \text{ even}. \end{cases} \quad (14)$$

The crucial step in NUFFT is the interpolation, as the accuracy of NUFFT approximation is heavily dependent on the quality of interpolator. In this paper, we adopt the min-max interpolation criterion detailed in [16] to design a high accuracy interpolator. Following the process of min-max interpolation criterion, we get the interpolator

$$\mathbf{u}(t_m) = \Lambda^H(t_m) [\mathbf{C}^H \mathbf{S} \mathbf{S}^H \mathbf{C}]^{-1} \mathbf{C}^H \mathbf{S} \mathbf{b}(t_m), \quad (15)$$

where $(\cdot)^H$ denotes the Hermitian transpose, $\mathbf{S} = \text{diag}\{a_n\}$, \mathbf{C} is an $N \times J$ matrix, $\Lambda(t_m)$ is a $J \times J$ diagonal matrix, and $\mathbf{b}(t_m)$ is an N -vector with respective entries

$$C_{nj} = \frac{e^{-i\gamma j(n-\eta_0)}}{\sqrt{N}}, \quad (16)$$

$$\Lambda_{jj}(t_m) = e^{i[2\pi t_m f_s/N - \gamma(k_m+j)]\eta_0}, \quad (17)$$

$$b_n(t_m) = \frac{e^{-i(2\pi t_m f_s/N - \gamma k_m)(n-\eta_0)}}{\sqrt{N}}, \quad (18)$$

where $\gamma = 2\pi/N$, $\eta_0 = (N-1)/2$.

By duality, we can realize NUFFT by reversing the steps described in (13). Note that the formula for interpolator in NUFFT is the same as (15), but the elements in each matrix and vector change to

$$\tilde{C}_{nj} = \frac{e^{-i\gamma[h(\tilde{k}_n+j)-h(j)](n-\eta_0)}}{\sqrt{N}}, \quad (19)$$

$$\tilde{\Lambda}_{jj}(\tilde{t}_m) = e^{i[2\pi \tilde{t}_m f_s/N - \gamma(\tilde{k}_n+j)]\eta_0}, \quad (20)$$

$$\tilde{b}_n(\tilde{t}_m) = \frac{e^{-i(2\pi \tilde{t}_m f_s/N - \gamma h(\tilde{k}_n))(n-\eta_0)}}{\sqrt{N}}, \quad (21)$$

where $h(m) = t_m f_s$, \tilde{t}_n , $n = 0, \dots, N-1$ is the uniform sampling instants, and the interpolator offset is

$$\tilde{k}_n = \begin{cases} \arg \min_{m \in \mathbb{Z}} |\tilde{t}_n - t_m| - (J+1)/2, & J \text{ odd}, \\ \max\{m \in \mathbb{Z} : \tilde{t}_n \geq t_m\} - J/2, & J \text{ even}. \end{cases} \quad (22)$$

4.2 Proposed NUFFT-IST scheme

Taking noise into account, we generally modify problem (3) into the following convex optimization problem

$$\min \|s\|_1 \quad \text{s.t.} \quad \|y - \Phi \Psi s\|_2^2 \leq \varepsilon, \quad (23)$$

where ε denotes the noise level. Such a constrained convex optimization problem can be transformed into the following non-constrained convex optimization problem

$$\min_s \frac{1}{2} \|y - As\|_2^2 + \varsigma \|s\|_1, \quad (24)$$

where ς is the regularization parameter. Although the target response s can be exactly recovered with high probability from measurements y by solving problem (24), it is quite computationally complex. Thus, a novel reconstruction algorithm based on NUFFT is proposed to achieve fast CS recovery by applying NUFFT to IST algorithm. IST is a state-of-the-art algorithm which has already been applied extensively to handle the unconstrained convex optimization problem arising in sparse signal recovery, image restoration and other linear inverse problems, which generates a sequence of estimates \hat{s}_k , $k = 1, 2, \dots$ to converge to the desired solution iteratively, i.e.,

$$\hat{s}_k = \text{soft}(\hat{s}_{k-1} + A^H(y - A\hat{s}_{k-1}), \varsigma), \quad (25)$$

where $\text{soft}(x, \varsigma) = \text{sign}(x) \max(|x| - \varsigma, 0)$ is the well-known soft-thresholding function. The detailed procedure of IST algorithm is described as follows:

- (1) Initialize $\hat{s}_0 = 0$, residual vector $r_0 = y$, and set iteration step $k = 1$.
- (2) Compute the current estimation: $\hat{s}_k = \text{soft}(\hat{s}_{k-1} + A^H r_{k-1}, \varsigma)$.
- (3) Update the residual vector: $r_k = y - A\hat{s}_k$.
- (4) Compute $f_k = 0.5\|r_k\|_2^2 + \varsigma\|\hat{s}_k\|_1$ and $\Delta f = |f_k - f_{k-1}|/f_{k-1}$. If $\Delta f \leq \delta$ then terminate the iteration. Otherwise, go to step (2) for the next iteration.

Like most CS reconstruction algorithms, the most time-consuming operation in IST algorithm is the matrix-vector multiplication involving A and A^H , with complexity of $\mathcal{O}(MN)$. Besides, each iteration requires two such multiplications. Therefore, the most critical problem in accelerating the IST recovery speed is reducing the computational complexity of the matrix-vector multiplication.

Fortunately, we find that if we expand the correlation computation

$$A^H r_{k-1} = A^H(y - A\hat{s}_{k-1}) = A^H y - B\hat{s}_{k-1}, \quad (26)$$

where $B = A^H A$ is an $N \times N$ matrix, the two multiplications decrease to one involving only B , and $A^H y$ is a constant vector that can be precomputed before the recovery. Although the computation cost of direct implementation increases from $\mathcal{O}(2MN)$ to $\mathcal{O}(N^2)$ along with the decrease in the number of multiplications, as mentioned above, A is composed of uniform and nonuniform DFT bases, which means we can accelerate the matrix-vector multiplication efficiently by making use of FFT algorithm. By (11) we rewrite $A^H A\hat{s}_{k-1}$ as

$$A^H A\hat{s}_{k-1} = F^H(v^* \odot (H^H H(v \odot (F\hat{s}_{k-1}))))). \quad (27)$$

Eq. (27) is more explicitly expressed as

$$A^H A\hat{s}_{k-1} = \text{IFFT}(v^* \odot \text{NUFFT}(\text{NUIFFT}(v \odot \text{FFT}(\hat{s}_{k-1}))))). \quad (28)$$

Now, the costly matrix-vector product is converted into a fast operation involving FFT, NUFFT and their corresponding inverse transforms. As a result, the computational complexity decreases from $\mathcal{O}(2MN)$ to $\mathcal{O}(4N \log N)$ which we will analyze in the following subsection.

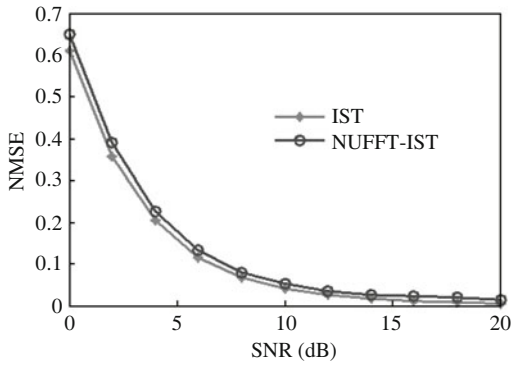


Figure 5 Normalized MSE versus SNR for NUFFT-IST and IST.

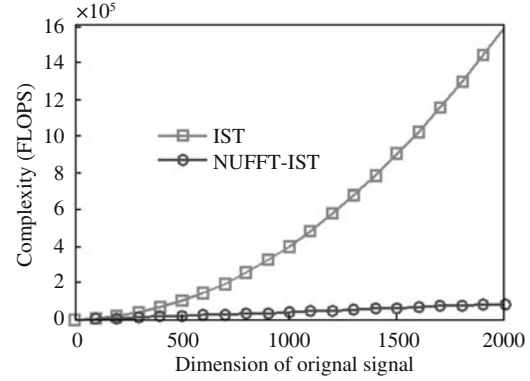


Figure 6 Computational complexity of NUFFT-IST and IST algorithm with 20% CS samples.

4.3 Computational complexity and performance of NUFFT-IST

It is impossible to accurately predict the number of iterations IST required to get the desired solution. The main operations per iteration include inner products, vector additions and the matrix-vector multiplication. However the former two require N operations which are negligible compared with the latter, so we only mention the cost of matrix-vector products per iteration in this paper.

By (15), obviously the interpolator only depends on the nonuniformly-spaced sampling instants rather than the original samples. In the IST algorithm, estimations \hat{s}_k generated in the recovery differ from each other, but the nonuniform sampling instants of measurements are fixed. So both NUFFT and NUIFFT in the proposed algorithm only need one fixed interpolator, which can be precomputed and stored before the signal recovery. According to [16], there are several methods for the interpolator precomputation. Take the QR decomposition for example. Precomputation for each sampling instant requires only $2JN$ operations.

In summary, excluding the interpolator precomputation, the overall operation count per NUFFT is $\mathcal{O}(N \log N + JN)$, while NUIFFT requires $\mathcal{O}(N \log N + JM)$ operations, where $\mathcal{O}(N \log N)$ is the complexity of the K -point oversampled FFT computation with $K = N$ in this paper, and $\mathcal{O}(JN)$, $\mathcal{O}(JM)$ are the cost of interpolations in NUFFT and NUIFFT respectively. As shown in (28), an N -point FFT and IFFT are required in each iteration, with $\mathcal{O}(2N \log N)$ operations in all. Accordingly, the computational complexity per iteration of NUFFT-IST is $\mathcal{O}(4N \log N + 2N + JM + JN)$, which is much lower than that of the conventional IST algorithm.

As for the storage requirement, we only need to store the interpolation coefficients and \mathbf{v} rather than store \mathbf{A} explicitly and consequently save lots of storage.

The normalized mean squared error (MSE) for NUFFT-IST and IST are given in Figure 5, where the results are the average over 200 runs. We see performance of NUFFT-IST is comparable to that of IST, in spite of the slight difference caused by the minimal approximation error of NUFFT. Figure 6 demonstrates the computational complexity of NUFFT-IST and conventional IST algorithm with 20% CS samples. It shows that the efficiency of NUFFT-IST algorithm is much higher than conventional IST algorithm. The complexity of the former is more than one order of magnitude simpler than the latter when the number of original signal samples exceeds 1000.

5 Experiment results

To validate the effectiveness of the proposed CS based spaceborne SAR wide-swath imaging scheme, first we give the imaging results of point targets simulation with doubled swath width by making use of system parameters of Radarsat-1 in F2 mode. Then we validate the effectiveness by interpolating and resampling the Radarsat-1 raw data in F2 mode. The corresponding parameters of the numerical simulations and raw data are shown in Table 1.

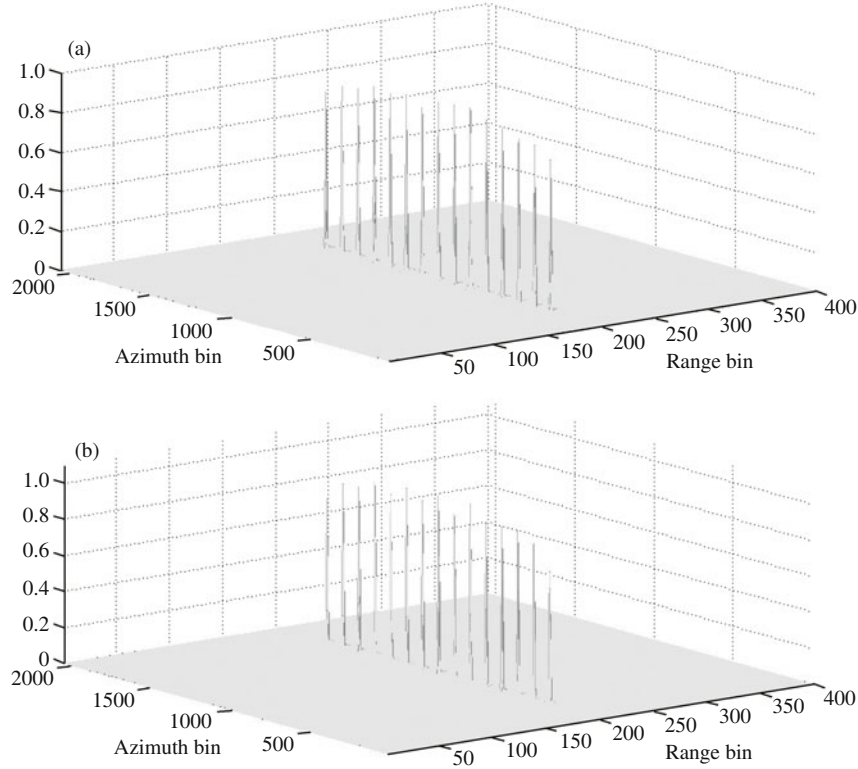


Figure 7 Imaging results of the point targets simulation. (a) The response of point targets at near range end of swath; (b) the response of point targets at far range end of swath.

According to system parameters in Table 1, the swath width restricted by PRF in F2 mode is 119.3 km. We can double the swath width with the Poisson disk-like azimuth sparse sampling pattern, and the first range bin of echo samples begins at $R_s = 980$ km. Set 15 point targets at the near range $R_1 = 989.3$ km and far range $R_2 = 1189.3$ km end of swath respectively (the distance between two targets is 560 m in azimuth direction), i.e., the whole swath width is $R_w = 238.7$ km.

The number of full samples sampled at PRF is 2048, while the number of sparse samples with Poisson disk-like sampling pattern is 822 after the swath width is doubled (Note that the number of Poisson disk random sequence generated each time is slightly different). Based on the CS-SAR imaging scheme described above, the response of point targets at near range end of swath is shown in Figure 7(a), while Figure 7(b) demonstrates the response of point targets at far range end of swath. We can see that the proposed Poisson disk-like sampling pattern based wide-swath CS-SAR imaging scheme provides imaging result with good performance of focusing and efficiently increase the swath width of conventional single channel spaceborne SAR system.

The Radarsat-1 raw data in F2 mode used in our experiment are obtained from the CD provided by [12]. The azimuth sample number of picked block data is $M_0 = 1536$. In order to implement the proposed nonuniform sampling pattern, we firstly interpolate the raw data in azimuth direction to increase the sampling rate with $q = 30$ times, and then resample the interpolated data by the Poisson disk-like nonuniform random sampling pattern, where the slow time of the new azimuth samples can be calculated by

$$t_j = t_{j-1} + \frac{2}{\text{PRF}} + \frac{m_j}{q\text{PRF}}, \quad (29)$$

where m_j is a random integer uniformly distributed in the interval $[0, q]$. And the initialization of t_0 is selected as $t_0 = 1/\text{PRF} + m_0/(q\text{PRF})$. The sampling pattern defined by (29) can ensure that the interval between any two adjacent samples is longer than $2/\text{PRF}$, meaning that the swath width can be increased one time. The imaging result of conventional method with full samples is shown in Figure 8(a), and Figure 8(b) illustrates imaging result with data sampled at a down sampling rate $\text{PRF}/2$, where the

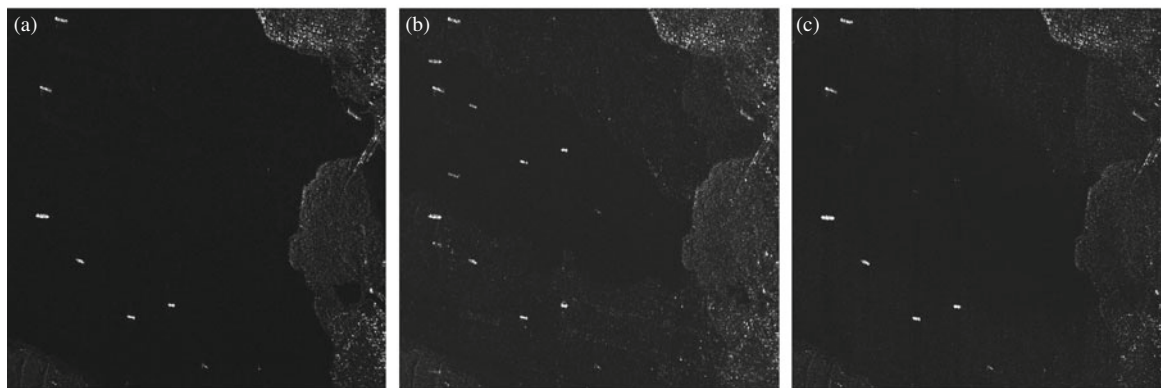


Figure 8 Imaging results with Radarsat-1 raw data. (a) Image obtained by conventional SAR imaging with full 1536 azimuth samples; (b) image obtained by conventional SAR imaging with a down sampling rate $PRF/2$, 768 azimuth samples; (c) image obtained by proposed Poisson disk-like sampling with 621 azimuth samples.

azimuth samples number is 768. Figure 8(c) shows the imaging result based on CS with the Poisson disk-like nonuniform samples mentioned above, and the corresponding azimuth samples number is 621. As shown in Figure 8, there exists obvious azimuth aliasing in Figure 8(b), while no such effect happens in Figure 8(c) even the samples used in Figure 8(c) are less than in Figure 8(b). Consequently, we can figure out that the proposed wide-swath imaging based on compressive sensing with Poisson disk-like sampling pattern is feasible and effective.

6 Conclusions

The new CS theory provides the possibility of increasing the swath width of conventional single channel spaceborne SAR system. The proposed Poisson disk-like nonuniform random sampling method in the azimuth direction allows for wider swath by restricting the smallest time interval between any two azimuth samples. The linear RMC is implemented while carrying out range compression through a similar way to the processing procedure of SPECAN algorithm, which can meet the demand for focusing with middle level imagery resolution. In the proposed SAR imagery method, azimuth focusing was taken as a CS reconstruction procedure. A novel fast CS reconstruction algorithm has been proposed for compressive sensing radar. By introducing the NUFFT and NUIFFT to IST algorithm, the proposed method replaces the direct matrix-vector products, and hence reduces the computational complexity efficiently. Experiment results validate the effectiveness of the proposed methods via the point target simulation and the Radarsat-1 raw data in F2 mode.

Acknowledgements

We thank professor Zhang Binchen and professor Hong Wen at national key laboratory of microwave imaging techniques, institute of electronics, CAS, for their help on the earlier draft of this paper. This work was supported by National Basic Research Program of China (Grant No. 2010CB731903), in part by National Natural Science Foundation of China (Grants No. 60901056, 61171122, 61001137), and Pre-research Project (Grant No. 9140C8001011001).

References

- 1 Currie A, Brown M A. Wide-Swath SAR. *IEE Proc F*, 1992, 139: 122–135
- 2 Gebert N, Krieger G, Moreira A. Digital beamforming on receive: Techniques and optimization strategies for high-resolution wide-swath SAR imaging. *IEEE Trans Aerosp Electron Syst*, 2009, 45: 564–592

- 3 Gebert N, Krieger G. Azimuth phase center adaptation on transmit for high-resolution wide-swath SAR imaging. *IEEE Geosci Rem Sens Lett*, 2009, 6: 782–786
- 4 Donoho D L. Compressed sensing. *IEEE Trans Inf Theory*, 2006, 52: 1289–1306
- 5 Candès E, Wakin M. An introduction to compressive sampling. *IEEE Signal Process Mag*, 2008, 25: 21–30
- 6 Baraniuk R, Steeghs P. Compressive radar imaging. In: *IEEE Radar Conference*, Boston, MA, 2007. 128–133
- 7 Herman M A, Strohmer T. High-resolution radar via compressed sensing. *IEEE Trans Signal Process*, 2009, 57: 2275–2284
- 8 Ender J H G. On compressive sensing applied to radar. *Signal Process*, 2010, 90: 1402–1414
- 9 Alonso M T, López-Dekker P, Mallorquí J J. A novel strategy for radar imaging based on compressive sensing. *IEEE Trans Geosci Rem Sens*, 2010, 48: 4285–4295
- 10 Potter L C, Ertin E, Parker J T, et al. Sparsity and compressed sensing in radar imaging. *Proc IEEE*, 2010, 98: 1006–1020
- 11 Quan Y, Zhang L, Guo R, et al. Generating dense and super-resolution ISAR image by combining bandwidth extrapolation and compressive sensing. *Sci China Inf Sci*, 2011, 54: 2158–2169
- 12 Cumming I G, Wong F. *Digital Processing of Synthetic Aperture Radar data: Algorithms and Implementation*. Norwood, MA: Artech House, 2005
- 13 Figueiredo M, Nowak R D. An EM algorithm for wavelet-based image restoration. *IEEE Trans Image Process*, 2003, 12: 906–916
- 14 Cook R L. Stochastic sampling in computer graphics. *ACM Trans Graph*, 1986, 5: 51–72
- 15 Vasanawala S S, Alley M T, Hargreaves B A, et al. Improved pediatric MR imaging with compressed sensing. *Radiology*, 2010, 256: 607–616
- 16 Fessler J A, Sutton B P. Nonuniform fast Fourier transforms using min-max interpolation. *IEEE Trans Signal Process*, 2003, 51: 560–574